Effect of long range order on sheared liquid crystalline materials: Flow regimes, transitions, and rheological phase diagrams

Tomohiro Tsuji and Alejandro D. Rey*
Department of Chemical Engineering, McGill University, 3610 University Street, Montreal, Quebec, Canada H3A 2B2
(Received 17 September 1999; revised manuscript received 18 September 2000)

A generalized theory that includes short-range elasticity, long-range elasticity, and flow effects is used to simulate and characterize the shear flow of liquid crystalline materials as a function of the Deborah (De) and Ericksen (Er) numbers in the presence of fixed planar director boundary conditions; the results are also interpreted as a function of the ratio R between short-range and long-range elasticity. The results are effectively summarized into rheological phase diagrams spanned by De and Er, and also by R and Er, where the stability region of four distinct flow regimes are indicated. The four regimes for planar (two-dimensional orientation) shear flow are (1) the elastic-driven steady state, (2) the composite tumbling-wagging periodic state, (3) the wagging periodic state, and (4) the viscous-driven steady state. The coexistence of the four regimes at a quacritical point is shown to be due to the emergence of a defect structure. The origin, the significant steady and dynamical features, and the transitions between these regimes are thoroughly characterized and analyzed. Quantitative and qualitative comparisons between the present complete model predictions and those obtained from the classical theories of nematodynamics (Leslie-Ericksen and Doi theories) are presented and the main physical mechanisms that drive the observed deviations between the predictions of these models are identified. The presented results fill the previously existing gap between the classical Leslie-Ericksen theory and the Doi theory, and present a unified description of nematodynamics.

PACS number(s): 64.70.Md, 47.50.+d, 47.54.+r

I. INTRODUCTION

It is well known that the classical theories for flowing liquid crystalline polymers predict that sheared nematic liquid crystalline (LC) materials have three typical flow regions with respect to the corresponding planar [two-dimensional (2D)] orientation modes: rotational (tumbling), oscillatory (wagging), and stationary (aligning) director orientations [1]; the Doi theory [2,3] for polymeric nematic flows also predicts log-rolling and kayaking out-of-plane orientation modes as well as above three in-plane modes [4]. All these flow regimes correspond to ideal homogeneous orientation fields, but in real situations liquid crystalline flows have bounding surfaces at which the orientation of the molecules are strongly affected by surfaces forces and torques. The presence of different and sometimes competing orienting tendencies arising from surface and flow effects activates long-range (Frank elasticity) forces and torques that may have a significant impact in the spatially nonhomogeneous structural process arising during flow. This type of analysis has been performed using the vector theory of Leslie and Ericksen (LE) [5], that neglects short-range elasticity and variations in the scalar order parameters. To complete the current understanding of flowing liquid crystalline materials, surfaces and long range elasticity must be included as in the LE theory but at the tensor level, thus taking into account all the bulk and surfaces effects and at the same time using a more detailed description of liquid crystalline orientation and order. Similar considerations apply to defects and disclinations, but these are outside the scope of this paper. Reviews of flow modeling of liquid crystalline materials are available in the literature [1,6–8].

Previously we presented a generalized flow model for liquid crystalline materials [9], that encompasses low molecular weight and polymeric nematics, and takes into account long- and short-range elasticity and flow-induced effects. The relative intensity of these three forces is captured by two dimensionless numbers, the Deborah (De) number (ratio of short range elasticity to viscous flow) and the Ericksen (Er) number (ratio of long range elasticity to viscous flow). It was shown [9] that when $\mathrm{Er}\rightarrow 0$ the model reduced to the Doi model with a closure approximation, and when $\mathrm{De}\rightarrow 0$ the model reduced to the Leslie-Ericksen theory (see the Appendix for details). As mentioned above, for planar (2D orientation) shear flows the classical Doi theory predicts three modes, and the LE theory predicts a flow aligning mode and a nonaligning mode. Since the high shear rate steady state predicted by the Doi theory is a flow aligning mode, it is equivalent to that predicted by the LE theory, except for the boundary layer regions. Thus any theory that encompasses the classical theories should, in the appropriate parametric limits of Er and De, predict four ideal flow modes (i.e., tumbling, wagging, flow aligning, and nonaligning), and explain the modifications of the ideal solutions for finite values of Er and De. The results presented below prove that the present model meets these criteria.

The objective of this paper are as follows. (1) To give a comprehensive characterization of all planar (2D) spatially inhomogeneous orientation modes of sheared nematic liquid crystalline materials predicted by the generalized model, for values of the governing Deborah and Ericksen numbers that include low molecular weight and polymeric liquid crystals (to facilitate the discussion in some cases we use the ratio R of short-range to long-range order as a dimensionless num-

*Email address: inaf@musicb.mcgill.ca

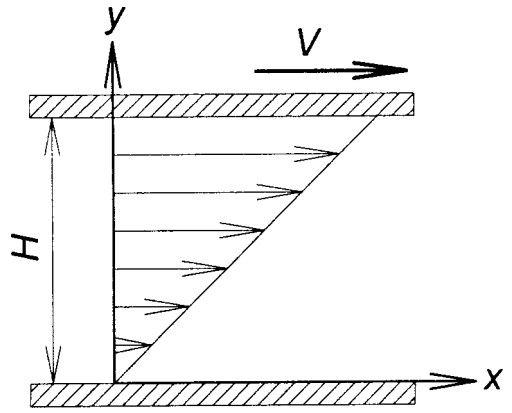

FIG. 1. Definitions of coordinate system and flow geometry. The liquid crystal sample is placed between two large flat parallel plates, and is sheared by moving the upper plate with a constant velocity V. At the bounding surfaces the tensor order parameter is a constant equal to its equilibrium value, and with the director parallel along the flow direction. The gap separation is H.

ber instead of the Deborah number). (2) To characterize and explain the driving mechanisms involved in the transitions between the various shear flow orientation regimes, and their dependence on the governing dimensionless number (De and Er, or R and Er). (3) To quantify and explain the deviations of the predictions of the present work from the classical solutions obtained using the LE theory and the Doi theory with the closure approximation. (4) To summarize the universal features of the in-plane shear rheology in terms of rheological phase diagrams span by the Deborah number and the Ericksen number, and by the ratio of short- to long-range elasticity and the Ericksen number.

The organization of this paper is a follows. Section II presents the scaled governing equations, dimensionless numbers, parameters, initial and boundary conditions, and the numerical methods used to solve the governing equations for a given shear flow. Section III presents and discusses the results given in terms of tensor order parameter profiles, director orientation angle profiles, and rheological phase diagrams. Section IV gives the main conclusions of this work.

II. GOVERNING EQUATIONS AND NUMERICAL METHODS

The rectilinear simple shear flow geometry studied in this paper is shown in Fig. 1, where H is the plate separation and V is the constant and given velocity of the moving upper plate; the bottom plate is fixed and the upper plate moves in the x direction. The shear plane is the x-y plane, and z is the vorticity axis. To characterize all the possible planar orientation modes we use the following tensor order parameter:

$$\mathbf{Q}=\int\left(\mathbf{uu}-\frac{\delta}{3}\right)f d\mathbf{u}^2=\begin{pmatrix} Q_{xx} & Q_{xy} & 0 \\ Q_{xy} & Q_{yy} & 0 \\ 0 & 0 & Q_{ZZ}\end{pmatrix}, \tag{1}$$

where $\mathbf{u}$ is a unit vector along a rodlike molecule, f is a orientation probability density function, and δ is the unit tensor. In terms of three eigenvalues $\{\mu_n,\mu_m,\mu_l\}$ and three eigenvectors $\{\mathbf{n},\mathbf{m},\boldsymbol{l}\}$, the orientation tensor is written as [10]

$$\mathbf{Q}=\mu_n\mathbf{nn}+\mu_m\mathbf{mm}+\mu_l\boldsymbol{ll}. \tag{2}$$

Commonly $\mathbf{n}$ is called the director, and the μ_i $(i=n,m,l)$ are related to the uniaxial scalar order parameter S and biaxial order parameter P, as follows [10]:

$$\mu_n=\frac{2}{3}S,\quad \mu_m=\frac{1}{3}(P-S),\quad \mu_l=-\frac{1}{3}(P+S). \tag{3}$$

For planar orientation modes, $\boldsymbol{l}$ is always collinear with the vorticity axis z. The evolution for the second order tensor $\mathbf{Q}$ in a flowing liquid crystalline material (see Ref. [9] for details) is given by the following dimensionless nonlinear coupled partial differential equations:

$$\begin{aligned}\frac{G\mathbf{Q}}{Gt^*}=&\frac{1}{\mathrm{De}}\left(-\frac{6}{(1-3/2\mathbf{Q}:\mathbf{Q})^2}\left\{\left(1-\frac{U}{3}\right)\mathbf{Q}\right.\right.\\&\left.-U\left[\mathbf{Q}\cdot\mathbf{Q}-\frac{1}{3}(\mathbf{Q}:\mathbf{Q})\delta\right]+U(\mathbf{Q}:\mathbf{Q})\mathbf{Q}\right\}\\&+\frac{1}{\mathrm{Er}}\left(\nabla^2\mathbf{Q}+\frac{L_2^*}{2}\left\{\nabla(\nabla\cdot\mathbf{Q})\right.\right.\\&\left.\left.+[\nabla(\nabla\cdot\mathbf{Q})]^T-\frac{2}{3}\mathrm{tr}[\nabla(\nabla\cdot\mathbf{Q})]\delta\right\}\right)+\frac{2}{3}\beta\mathbf{A}^*\\&+\beta\left\{\mathbf{A}^*\cdot\mathbf{Q}+\mathbf{Q}\cdot\mathbf{A}^*-\frac{2}{3}(\mathbf{A}^*:\mathbf{Q})\delta\right\}\\&-\frac{1}{2}\beta\{(\mathbf{A}^*:\mathbf{Q})\mathbf{Q}+\mathbf{A}^*\cdot\mathbf{Q}\cdot\mathbf{Q}+\mathbf{Q}\cdot\mathbf{A}^*\cdot\mathbf{Q}+\mathbf{Q}\cdot\mathbf{Q}\cdot\mathbf{A}^*\\&-[(\mathbf{A}^*\cdot\mathbf{Q}):\mathbf{Q}]\delta\},\end{aligned} \tag{4}$$

where G/Gt is the corotational derivative, L_2^* is a dimensionless Landau coefficient [11], β is a shape factor [10,12], U is a dimensionless nematic potential intensity, $\mathbf{A}^*$ is a rate of strain tensor, and where a superposed star denotes a dimensionless quantity. The original variables are nondimensionalized using the plate separation distance H, the upper plate velocity V, and the Landau coefficient L_1 [9] as characteristic values for distance, velocity, and energy per unit length, respectively. De and Er are the Deborah and Ericksen numbers defined as

$$\mathrm{De}=\frac{V}{D^*H}, \tag{5a}$$

$$\mathrm{Er}=\frac{\eta HV}{L_1}, \tag{5b}$$

where D^* is a rotational diffusivity coefficient, and η is a viscosity. The first group in the right side of Eq. (4) (i.e., the terms multiplied by 1/De) represent the nematic short-range order, the second (i.e., the terms multiplied by 1/Er) the long-range order (Frank elasticity), and the last the viscous flow effect. Thus, the two dimensionless numbers give the ratio of the three processes (i.e., long-range, short-range, and viscous flow), with De being the ratio of the viscous to short-range elastic effect, and Er the ratio of viscous effect to long-range elastic effect. However, since both Er and De

include the shear rate (V/H), both numbers are changed by changing the operating conditions (shear rate). In some instances it is preferable to discuss and analyze the results using a dimensionless number independent of the shear rate. A convenient dimensionless number is the ratio of Er to De,

$$R=\frac{\mathrm{Er}}{\mathrm{De}}=\frac{\eta H^2 D^*}{L_1}, \tag{5c}$$

which gives the relative magnitude of short-range to long-range elastic effects, and also represents the ratio of the time scales for change in the eigenvalues of $\mathbf{Q}$ to the time scale for changes in the eigenvectors of $\mathbf{Q}$. Another interpretation of R is that it is the square of the ratio of the system length scale (H) and the mesoscopic length scale ξ [$\xi=(L_1/D^*\eta)^{1/2}$]. By introducing R, Eq. (4) becomes

$$\begin{aligned}\mathrm{Er}\frac{G\mathbf{Q}}{Gt^*}=R\Bigg(&-\frac{6}{(1-3/2\mathbf{Q}:\mathbf{Q})^2}\Bigg\{\left(1-\frac{U}{3}\right)\mathbf{Q}\\&-U\left[\mathbf{Q}\cdot\mathbf{Q}-\frac{1}{3}(\mathbf{Q}:\mathbf{Q})\,\delta\right]+U(\mathbf{Q}:\mathbf{Q})\mathbf{Q}\Bigg\}\Bigg)\\&+\nabla^2\mathbf{Q}+\frac{L_2^*}{2}\Bigg\{\nabla(\nabla\cdot\mathbf{Q})+[\nabla(\nabla\cdot\mathbf{Q})]^T\\&-\frac{2}{3}\mathrm{tr}[\nabla(\nabla\cdot\mathbf{Q})]\,\delta\Bigg\}+\mathrm{Er}\Bigg(\frac{2}{3}\beta\mathbf{A}^*\\&+\beta\Bigg\{\mathbf{A}^*\cdot\mathbf{Q}+\mathbf{Q}\cdot\mathbf{A}^*-\frac{2}{3}(\mathbf{A}^*:\mathbf{Q})\,\delta\Bigg\}\\&-\frac{1}{2}\beta\{(\mathbf{A}^*:\mathbf{Q})\mathbf{Q}+\mathbf{A}^*\cdot\mathbf{Q}\cdot\mathbf{Q}+\mathbf{Q}\cdot\mathbf{A}^*\cdot\mathbf{Q}\\&+\mathbf{Q}\cdot\mathbf{Q}\cdot\mathbf{A}^*-[(\mathbf{A}^*\cdot\mathbf{Q}):\mathbf{Q}]\,\delta\}\Bigg).\end{aligned} \tag{6}$$

The chosen values for the physical parameters used throughout this work are as follows: shape factor $\beta=0.9$ [12], nematic potential intensity $U=6$, Landau coefficient $L_2^*=1/2$ (this corresponds to the Frank elasticity coefficients $K_1=K_3=3K_2$, in the case of a uniaxial nematic). Equation (4) is solved using a fourth order Runge-Kutta method for time integration and a second order finite difference method for the spatial discretization. Also, the computational conditions are: Runge-Kutta time step width $\Delta t^*=10^{-3}$, and spatial discretization width $\Delta y^*=10^{-2}$. The initial and boundary conditions used throughout are

$$\begin{aligned}\mathbf{Q}(t=0,0\leqslant y^*\leqslant 1)&=\mathbf{Q}(t>0,y^*=0)\\&=\mathbf{Q}(t>0,y^*=1)\\&=S^{\mathrm{eq}}\left(\mathbf{n}_s\mathbf{n}_s-\frac{\delta}{3}\right),\end{aligned} \tag{7}$$

where the uniaxial order parameter at equilibrium S^{eq}, and director $\mathbf{n}_s$ at the bounding surfaces are given by

$$S^{\mathrm{eq}}=\frac{1}{4}+\frac{3}{4}\sqrt{1-\frac{8}{3U}},\quad \mathbf{n}_s=\begin{pmatrix}1\\0\\0\end{pmatrix}. \tag{8}$$

The surface director $\mathbf{n}_s$ is always aligned along the x direction and the surface scalar order parameters is equal to the equilibrium value S^{eq}, and thus prior to the imposition of flow the system is spatially homogeneous and at the lowest energy state. The boundary conditions used here can be altered by treating the surface as viscoelastic, as done by Rey [13]. To facilitate the analysis and discussions of the computational results we use 2D plots as well as scientific visualizations of the tensor order parameter profiles as a function of dimensionless time. The tensor order parameter is represented by an ellipse, whose major (minor) axis represents $\mathbf{n}$ ($\mathbf{m}$) and whose axes lengths are proportional to μ_n and μ_m, respectively.

III. RESULTS AND DISCUSSIONS

A. Four flow regimes

After an extensive computational investigation of Eqs. (4), (7), and (8), it has been found that the present model predicts four distinct flow regimes as the dimensionless values R and Er (or De and Er) are varied through the interval [0, ∞), in agreement with the restrictions imposed by the classical solutions mentioned in the introduction. The four flow regimes within the planar orientation restriction are (a) elastic-driven steady state (ESS), (b) composite tumbling-wagging periodic state (TWS), (c) wagging periodic state (WS), (d) viscous-driven steady state (VSS). The existence of four flow regimes can be qualitatively explained by considering the effects of the governing dimensionless numbers R and Er. If Er is sufficiently small, the ESS steady state always prevails for any R because long-range elasticity dominates over flow effects. If R is sufficiently small, the eigenvalues of $\mathbf{Q}$ are strongly affected by moderately strong flows, an effect that quenches the rotational tendencies of shear, and eventually leads at sufficiently large Er to flow-alignment or VSS mode. If R is sufficiently large the eigenvalues of $\mathbf{Q}$ are relatively insensitive to the flow strength, such that increases in Er increases the rotational effects of the flow, giving rise to the emergence of the tumbling (TWS) and wagging (WS) periodic modes, and finally at high Er to flow-alignment (VSS). Thus at lower R increasing Er produces a transition between two steady states: ESS→VSS. On the other hand at higher R, increasing Er produces the following cascade: ESS→TWS→WS→VSS. In this section we present, characterize, and discuss these four distinct shear flow regimes, while the transitions are considered in Sec. III C. In what follows we show the necessary and sufficient results that meet the objective of this paper (see the Introduction).

(a) *Elastic-driven steady state (ESS)*. The elastic-driven steady state arises when the stabilizing effect of the long-range order overcomes the rotating effects due to the vorticity of the flow and arises for sufficiently small Er and arbitrary R. This low Er regime was discussed at length in Ref. [9], and here we summarize the most important features.

Figure 2 shows the director angle θ at the center line ($y^*=0.5$) as a function of dimenstionless time t^*, for R

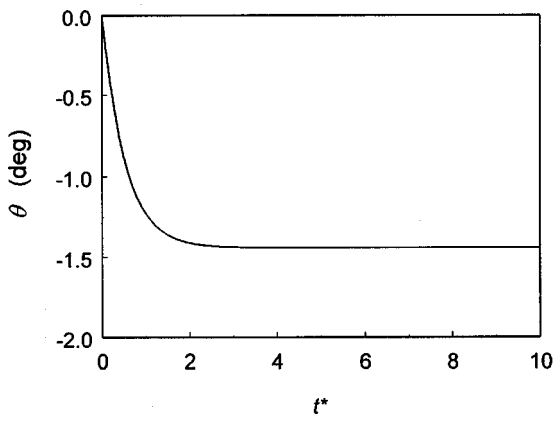

FIG. 2. Director angle θ at the center line ($y^*=0.5$) as a function of Er for $R=250$ (solid line) and 2500 (dotted line). The profiles (Er=206 for $R=250$ and Er=629 for $R=2500$) end at the ESS-TWS transition. The solution multiplicity is similar to that predicted by LE theory.

$=100$ and Er$=10$ (De$=0.1$). The shown figure is typical and representative of the ESS regime. The director angle decreases monotonically to a steady state. In the absence of long range order the director would tumble according to the Doi theory with the closure approximation since for the present case the tumbling-wagging transitions occurs at De ≈ 25 and the wagging-steady state transition occurs at De ≈ 58. However, in a spatially inhomogeneous system the long-range elasticity is able to frustrate the director periodic motion. In the ESS regime Frank elasticity dominates over the entire flow geometry and this corresponds to a director profile with a nonvanishing first derivative $\partial\theta/\partial y^*=0$ (a typical profile discussed in detail later is shown by the dotted line in Fig. 6). Figure 3 shows the director angle θ at the center line ($y^*=0.5$) as a function of Er, for $R=250$ (solid line) and 2500 (dotted line). The profiles exist up to Er* $=206$ for $R=250$, and Er* $=629$ for $R=2500$, respectively, since the ESS-TWS transition occurs at these critical Er* (The transition is discussed in detail in Sec. III C). This means that for $R=250$, if Er$<$Er*$\leqslant$206, ESS is the stable solution to Eq. (4), and if Er$>$Er*$=$206 ESS does not exist, and TWS is the stable solution; identical statements apply to

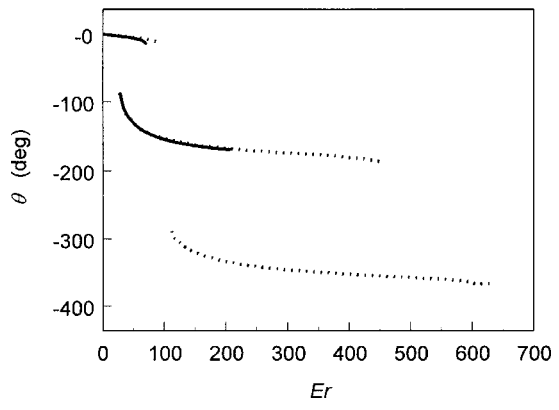

FIG. 3. Director orientation angle θ as a function of dimensionless time t^* at the center line ($y^*=0.5$), for Er$=10$ and $R=100$. The shown figure is typical and representative of the ESS regime. The director dynamics is overdamped.

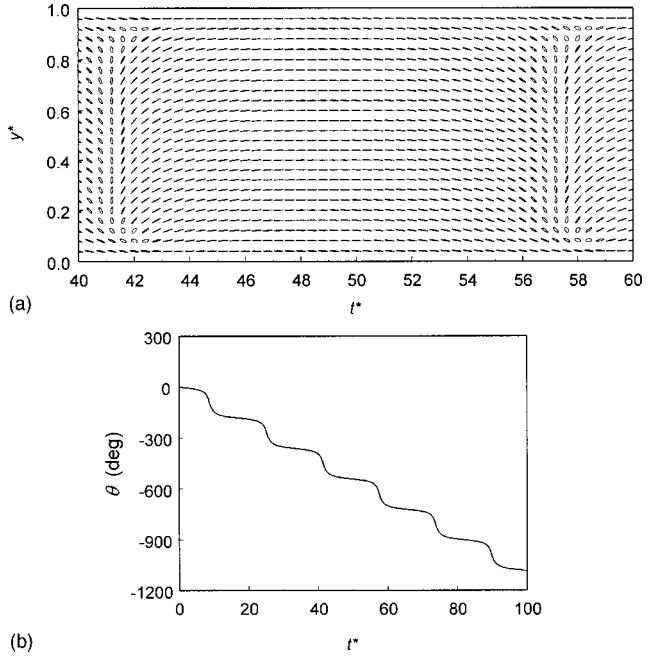

FIG. 4. (a) Scientific visualization of the tensor order parameter ellipsoid profiles as a function of dimensionless time t^*, (b) director orientation angle θ as a function of dimensionless time t^* at the center ($y^*=0.5$). The parametric conditions are $R=100$ and Er $=2000$ (De$=20$), and is typical and representative of the TWS regime. In the two surface layers found between the bounding surfaces and the abnormal state, the director oscillates in time, and in the bulk region the director rotates clockwise.

$R=2500$ but with Er* $=629$. As Er increases from zero, the director exhibits discontinuous jumps at Er$=75$ for $R=250$, and at Er$=75$ and 541 for $R=2500$. As Er decreases from 700 the discontinuous jumps occurs at Er$=29$ for $R=250$, and at Er$=27$ and 112 for $R=2500$. The solution multiplicity displayed by the present model is similar to that predicted by the LE theory [14], with the important difference that the ESS solutions exist up to a certain critical R-dependent value of the Ericksen number Er*(R). As R increases the range of existence of ESS increases and as $R\rightarrow+\infty$, the ESS mode exist for all Er, in agreement with the fact that the present model converges to the LE model as $R\rightarrow+\infty$.

The main features of the ESS regime are (1) the orientation field reaches a steady state, (2) the transient process to its steady state is monotonic and nonoscillatory, (3) the steady states arises due to the long-range elasticity, (4) under the same conditions a homogeneous system displays the tumbling state (or wagging state if De is sufficiently large), (5) higher values of R and lower values of Er promote the appearance of this state, (6) the difference between the present predictions and the LE solutions for tumbling nematics is that in the present case the steady state solutions disappear at a R dependent critical Er*, while they always exists for the LE model, and (7) in the ESS regime there is no orientation boundary layer behavior because there is no flow alignment in the bulk.

(b) *Composite tumbling-wagging periodic state (TWS).* The TWS time periodic regime exist at sufficiently large R and Er. Figure 4(a) shows a computed scientific visualization

of the tensor order parameter ellipsoid profiles as a function of dimensionless time t^*, for $R=100$ and Er$=2000$ (De $=20$). The shown figure is typical and representative of the TWS regime. The figure shows that in the core region (around $y^*\approx 0.5$) the ellipsoids rotate (tumbling mode) as function of time and that in the two layers close to the two bounding surfaces ($y^*=0$, $y^*=1$) the ellipsoids oscillate (wagging mode) with a space dependent amplitude; the amplitude decreases to zero at the bounding surfaces and increases to a maximum value at the boundary between these tumbling and wagging regimes. The term composite in the subtitle of this section refers to the fact that two different (i.e., rotational and oscillatory) time dependent modes coexist spatially, with the tumbling layer occupying the center region ($y^*=0.5$) and the two wagging layers adjacent to the bounding surfaces ($y^*=0,1$). The thickness of the two wagging layers decrease with increasing Er.

Figure 4(b) shows the director angle θ at the centerline ($y^*=0.5$) as a function of dimensionless time t^*, for $R=100$ and Er$=2000$ (De$=2$). The shown periodic evolution is typical and representative of this regime. The director in the bulk region rotates continuously with time, and displays the classical steplike time evolution [1]. As shown in Fig. 3(a) the director near the bounding surfaces oscillates (wagging layers). To smoothly and continuously connect the director periodic rotation in the bulk region with the oscillatory motion in the two wagging layers, the ellipsoids periodically becomes circles [6] at the two boundaries between the core tumbling region and the two wagging surface layers. When the ellipsoid becomes a circle, the μ_n and μ_m eigenvalues of **Q** are equal, a configuration known as the abnormal nematic state [15]. The periodic emergence of the two abnormal nematic states creates a director resetting mechanism that allows the presence of a core tumbling layer in the presence of fixed boundary orientation in a sheared nematic sample without creation of persistent singularities or defects. The incompatibility of the strong anchoring condition with the bulk tumbling behavior was foreseen by Marrucci [16], using the vector type equation.

When Er$\rightarrow+\infty$ due to absence of long-range elasticity the TWS mode becomes identical to the tumbling mode predicted by the Doi theory with the closure approximation (and $\beta=0.9$), but at finite Er the TWS mode is drastically different for Doi's tumbling mode at the same De values, as shown by Fig. 4(a). The main features of the composite tumbling-wagging state are (1) the director dynamics in the bulk region is rotational, and oscillatory in the two surface layers, (2) at the two boundaries between these three regions the abnormal nematic state emerges periodically, (3) the tensor order parameter **Q** corresponding to the abnormal nematic state has two equal eigenvalues ($\mu_n=\mu_m$) and the director **n** is undefined. This creates a director resetting mechanism.

(c) *Wagging periodic state (WS)*. The WS periodic regime exists at sufficiently large R and Er. Figure 5(a) shows a computed scientific visualization of the tensor order parameter profiles as a function of dimensionless time t^*, for $R=100$ and Er$=3000$ (De$=30$). The figure is typical and representative of this regime. If Er is sufficiently large a new wagging periodic regime emerges and replaces the tumbling core region found in this regime for lower Er numbers [see

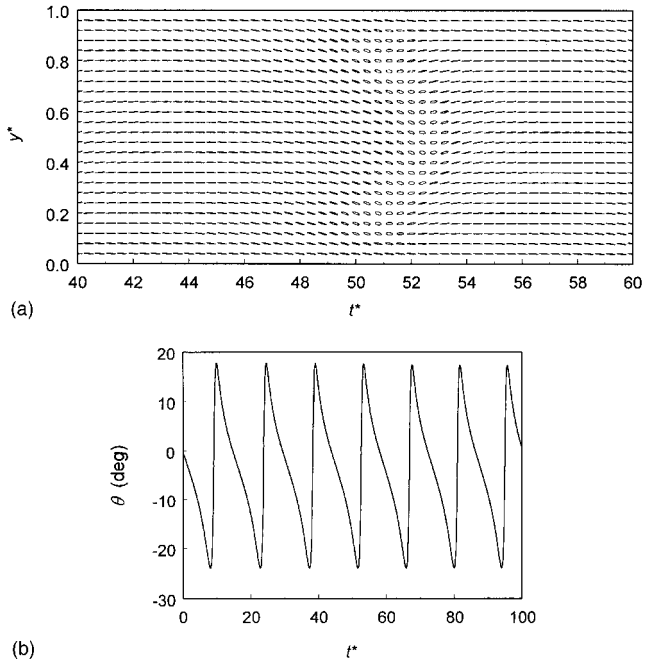

FIG. 5. (a) Scientific visualization of the tensor order parameter ellipsoid profiles as a function of dimensionless time t^*, (b) director orientation angle θ as a function of dimensionless time t^* at the center ($y^*=0.5$). The parametric conditions are $R=100$ and Er $=3000$ (De$=30$), and is typical and representative of the WS regime. The ellipsoids oscillates periodically, with an amplitude that is a maximum at the centerline and zero at the boundary surfaces.

(b)]. The figure shows the periodic oscillations of the ellipsoids, with an amplitude that is a maximum at the centerline and zero at the bounding surfaces, where a fixed orientation is imposed through the boundary conditions. Figure 5(b) shows the director angle θ at the centerline ($y^*=0.5$) as a function of dimensionless time t^*, for $R=100$ and Er $=3000$ (De$=30$), and represents the typical behavior in this flow regime. The flow regime is periodic with the director always close to the flow direction. The scalar order parameters changes seen at $t^*\approx 52$ in Fig. 5(a) are due to the fact that at this time the difference between the bulk director orientation and the flow direction is a maximum, as seen in Fig. 5(b) at $t^*\approx 52$ (see Farhoudi and Rey [17] for details). A direct comparison between Figs. 4 and 5 reveals the sources of the major differences between the TWS and WS. In the TWS the difference between the director angle in the bulk region and at the boundary surfaces increases continuously with time. On the other hand, in the WS the director oscillates with bounded (less than π radians) amplitude and thus the difference between the bulk director angle and the surface director angle is always finite, and no abnormal nematic emerges because no resetting mechanism is needed to make the bulk dynamics compatible with the fixed surface orientation.

The WS regime becomes identical to that predicted by the Doi theory with the closure approximation (and $\beta=0.9$) when Er$\rightarrow+\infty$. For finite Er the WS is spatially inhomogeneous while Doi's wagging regime is homogeneous. The main features of the WS are (1) the director dynamics over the entire flow geometry is periodic oscillatory, with an amplitude that decreases from a maximum at the centerline to

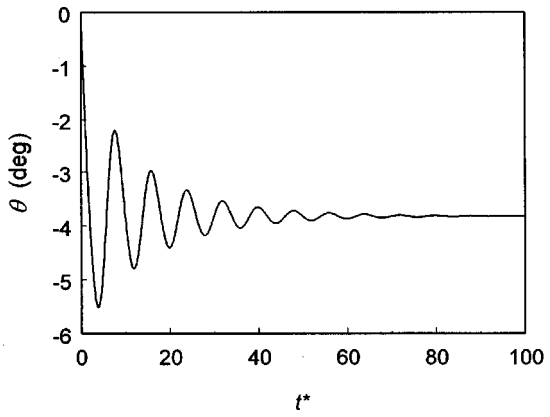

FIG. 6. Director orientation angle θ as a function of dimensionless time t^* at the center ($y^*=0.5$), for Er$=10000$ and $R=100$. The shown figure is typical and representative of the VSS regime. The director dynamics is underdamped.

zero at the bounding surfaces, (2) for a given R the period decreases with increasing Er.

(d) *Viscous-driven steady state (VSS)*. At sufficiently large Er and appropriate R (see Sec. III B) the flow regime is steady. The steady state is driven by the viscous flow and is different to the ESS in many significant aspects.

Figure 6 shows the director orientation angle θ at the centerline ($y^*=0.5$) as a function of dimensionless time t^*, for $R=100$ and Er$=10000$ (De$=100$). The shown figure is typical and characteristic of this regime. The evolution in the VSS regime is underdamped in contrast to being overdamped in the ESS regimes. To highlight the significant differences between these two steady state regimes (ESS and VSS), Fig. 7 shows the steady state director profiles $\theta(y^*)$ for ESS (solid line, $R=100$, Er$=10$, and De$=0.1$) and for VSS (dotted line, $R=100$, Er$=10000$, and De$=0.1$). The director profile for ESS is parabolic, and for VSS displays the classical boundary layer behavior, with rapid changes near the bounding surfaces and a flat profile in the core. The shape of the profiles is dictated by the nature of the stabilizing mechanism that promotes the steady state. For ESS the steady states arises due to the long range elasticity effect that

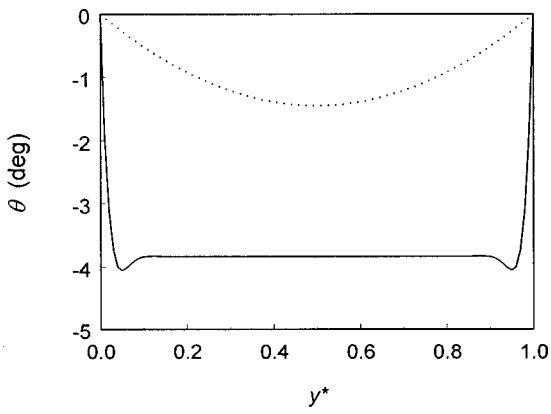

FIG. 7. Steady state director profiles $\theta(y^*)$ for ESS (solid line, $R=100$, Er$=10$, and De$=0.1$) and for VSS (dotted line, $R=100$, Er$=10000$, and De$=0.1$). The director profile for ESS is parabolic, and for VSS displays boundary layer behavior with rapid changes near the bounding surfaces and a flat profile in the core.

is activated in spatially inhomogeneous director fields. On the other hand, VSS is driven by the viscous flow orienting effect and is independent of the long range elasticity. The flow aligning angle typical of the VSS regime and known as the Leslie angle in the LE theory is for this case approximately $-4°$.

In the context of the classical theories the director profile in the ESS regime is similar to that predicted by the LE theory for non-aligning nematics, while the director profile in the VSS regime is similar to that predicted by the LE theory for aligning nematics (note that the classical uniaxial LE theory predicts positive flow-aligning angles). As Er$\rightarrow+\infty$ due to the absence of long range elasticity the VSS regime is identical to that predicted by Doi theory with the closure approximation (and $\beta=0.9$). Introducing long-range elasticity introduces deviations from Doi theory, with the orientation boundary layers being the most important. The main features of the VSS regime are (1) the steady director profile displays a typical boundary layer behavior, where the bulk is dominated by the flow-orienting torque that align the director close to the flow direction, (2) the transients are underdamped, (3) the driving force to achieve steady state is the viscous flow, and is completely different from the ESS which is driven by long-range elastic torques.

B. Rheological phase diagram

The rheological phase diagram is a two-dimensional plot that displays all the stable flow regimes as a function of the governing dimensionless numbers R and Er (or De and Er). In this study we have performed a comprehensive solution characterization in the two parameter planes, and below show results using the following symbols to denote the stable solutions to Eqs. (4), (7), and (8) for the given values of R and Er (or De and Er): squares for ESS, diamonds for VSS, triangles for WS, and open circles for TWS. Due to the complexity of the nonlinear system of coupled partial differential equations no method to compute the exact boundary between the different flow regimes was found, but the large number of computed solutions gives a sufficiently accurate location of the transition lines in the parametric plane.

Figure 8 shows the rheological phase diagram containing the stable regions of the four ESS, TWS, WS, and VSS flow regimes as a function of R and Er. The closed circle denotes a quacritical point from which the four transition lines (i.e., line separating two regimes) emanate. Since as mentioned above no lines were computed, they are not explicitly shown but are clearly apparent in the figure. The location of the quacritical point is $(R,\mathrm{Er})\approx(3.8,60)$, and at this point the four flow regimes coexist (see discussion in Sec. III C). For $R>3.8$ the system displays the four flow regimes as Er increases. However for $R<3.8$ only steady states (ESS and VSS) are found. The TWS and WS regions shrink as the quacritical point is approached and are extinguished at that point. The reason why the TWS and WS region disappear as R and Er decrease towards the quacritical point is that both numbers scale with the inverse of the long-range elasticity which tends to damp any periodic behavior. The ESS region spreads to higher Er as R increases. For high R the scalar order parameter [S, see Eq. (3)] remains relatively unaffected by the flow and close to its equilibrium value, and a rela-

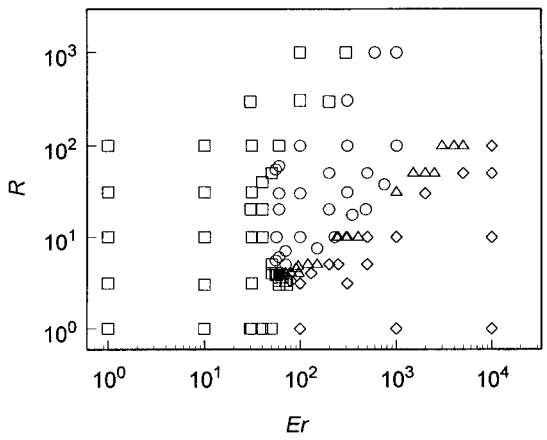

FIG. 8. Rheological phase diagram as a function of R and Er. The figure shows the stable regions of the four ESS (□), TWS (○), WS (△), and VSS (◇) flow regimes. (●) denotes a quacritical point from which the four transition lines (i.e., line separating two regimes) emanate.

tively higher Er is needed to activate the rotational dynamics of the tumbling state though the emergence of the abnormal nematic state. At sufficiently low R, and sufficiently high Er the decrease of the scalar order parameter produces the emergence of the VSS, known as the flow aligning regime in the LE theory [5]. As mentioned above the mechanism that produces the emergence of VSS through a decrease of S and an increase of the reactive order parameter [6] to a value greater than 1 is explained in Ref. [17]. The reason why the VSS region widens with increasing R and Er is that as R increases higher flow strength (higher Er) is required to produce the scalar order parameter changes that produce the flow aligning regime. In terms of the classical theories, the LE limit is approached when $R \rightarrow +\infty$ where the only solution is ESS, and the Doi limit is approached when $\mathrm{Er} \rightarrow +\infty$, where TS, WS, and VSS are the stable solutions.

Figure 9 shows the rheological phase diagram in terms of De and 1/Er; the symbol notation corresponds to that of Fig. 8. The quacritical point is located at $\mathrm{De, Er} = (15.8, 60)$. It is useful to note that the vertical axis represent the predictions

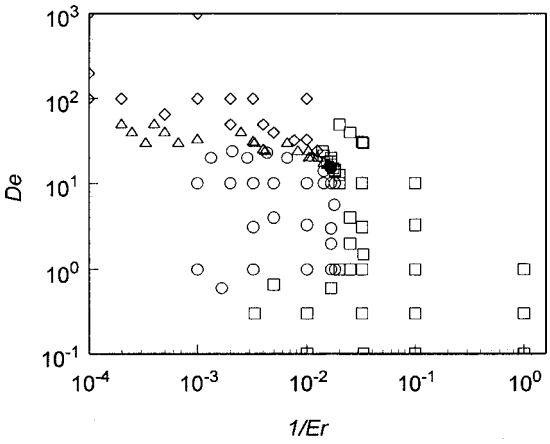

FIG. 9. Rheological phase diagram as a function of De and 1/Er. The figure contains the stable regions of the four ESS (□), TWS (○), WS (△), and VSS (◇) flow regimes, and a quacritical point (●). See text.

of the Doi model with the closure approximation (and $\beta = 0.9$), while the horizontal axis represent the predictions of the LE model for a nonaligning nematic [17]. In Sec. I we showed that the present model converges to the Doi model when $\mathrm{Er} \rightarrow 0$ (spatially homogeneous system), where no ESS exists, and the tumbling-wagging and wagging-aligning transitions occurs at $\mathrm{De} \approx 25$ and 58, respectively, in agreement with Fig. 8. For $\mathrm{De} \rightarrow 0$, the system has no periodic states, in agreement with the well-known LE solutions. Increasing 1/Er the periodic TWS and WS regions become smaller and finally disappear at $1/\mathrm{Er} \geqslant 0.016$. In Fig. 8 the strength of the long-range order increases with increasing 1/Er, so that the right-hand side of Fig. 9 corresponds to the lower left side of Fig. 8.

C. Flow regimes transitions

In this section we characterize and discuss the transitions between the four flow regimes, especially the ESS-TWS transition, and the quacritical point. As shown in the rheological phase diagrams (Figs. 8 and 9), there are four kinds of transition lines in the parametric plane corresponding to (a) ESS-TWS, (b) TWS-WS, (c) WS-VSS, and (d) ESS-VSS transitions. As mentioned above, while we could not find the exact location of transition lines due to lack of a numerical technique, they do converge at a point (here denoted the quacritical point as in equilibrium phase transitions [18]), as unambiguously shown in Figs. 8 and 9.

The bifurcation analysis of a similar model as used here in a homogeneous system has been performed by Farhoudi and Rey [17]. They have established the mechanism of transition between tumbling and wagging modes and the bifurcation involved in the transition between the wagging and aligning orientation modes. It is shown [17] that the tumbling orbit splits into two limit cycles at the TWS-WS transition point, and then at higher De a Hopf bifurcation sets in at WS-VSS transition point. To analyze the transitions in the present model we use the following fact: since the main features of the system depend on the bulk region behavior where the long range elasticity has comparatively less effect than close to the surfaces, using the results of Ref. [17] to analyze mode transitions in the inhomogeneous system studied here is appropriate and accurate, unless the transition includes the ESS mode. The four transitions and the qua-critical point are analyzed in what follows.

(a) *ESS-TWS transition*. The time period of the orientation dynamics of the TWS mode diverges at the transition point. In Ref. [9] we characterized the director rotation time period in the TWS regime, and established the divergence of the time period at this transition line. The orientation phenomena at the ESS-TWS transition is deduced from the behaviors of $\mathbf{Q}$ in both the ESS and TWS mode in the immediate vicinity of the transition. Figure 10(a) shows the director angle θ at the center line ($y^* = 0.5$) as a function of dimensionless time t^*, for $R = 100$ and $\mathrm{Er} = 85$ ($\mathrm{De} = 0.85$), for the TWS mode very close to the ESS-TWS transition line. The angle profile shows a novel director rotation behavior where the director has a two-step-like change in a single period. The corresponding computed scientific visualization of the tensor order parameter profiles as a function of dimensionless time is shown in Fig. 10(b). From these figures it can be seen that

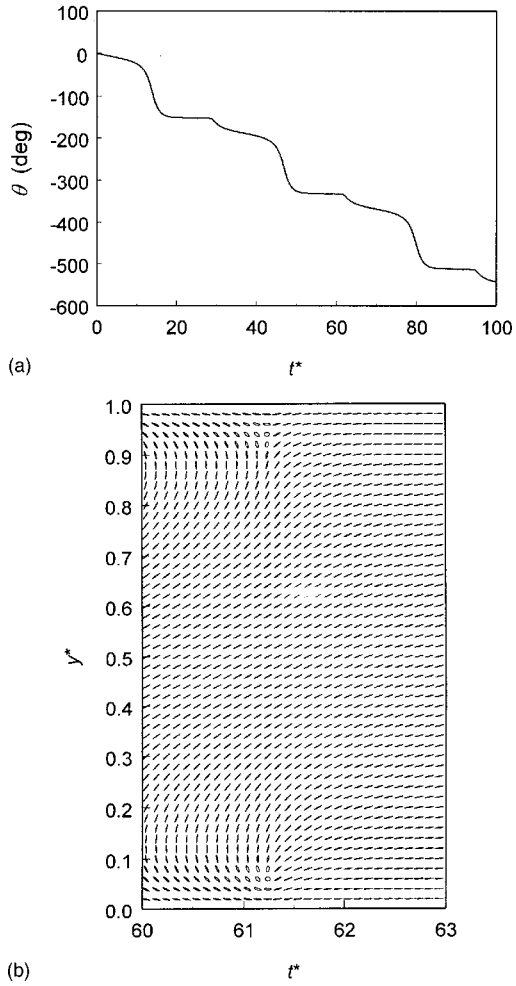

FIG. 10. (a) Director angle θ at the centerline ($y^*=0.5$) as a function of dimensionless time t^*, (b) scientific visualization of the tensor order parameter ellipsoid profiles as a function of dimensionless time t^*, for $R=100$ and Er$=85$ (De$=0.85$). The figures show the TWS mode very close to the ESS-TWS transition line; $\theta(y^*=0.5,t^*)$ shows a novel director rotation behavior where the director has a two-step-like change in a single period. The small step is strongly correlated to the emergence of the abnormal nematic state.

the director rotation behavior is strongly related to the appearance of the abnormal nematic state. For example, the short step at $t^*\approx 61.2$ in Fig. 10(a) reflects the emergence of the two abnormal states close to the bounding surfaces in Fig. 10(b). In the usual tumbling case, the director's angular velocity accelerates when the director is perpendicular to the flow direction, and decelerates when the director is close to the flow direction. However, near the ESS-TWS transition the angular velocity decelerates and accelerates just before and after the appearance of the abnormal nematic state. On the ESS side of the transition, the orientation field requires infinite time to reach steady state and the steady state profile includes two states which are almost abnormal nematic states. On the TWS side near the transition the abnormal nematic states appear before the system reaches the steady state. Before the appearance of the abnormal nematic state, the viscous flow effect is almost balanced by the long-range elastic contribution, and thus the torque on the director becomes low. The appearance of the abnormal nematic changes the spatial arrangement of the director rotation from clockwise to counterclockwise, so that the sign of the long-range elasticity contribution also changes from positive to negative, explaining why in the TWS mode rotation prevails in the bulk of the sample. The short step in the center line director evolution fades away when moving away from the transition line (i.e., changing Er and De), since the elastic and viscous effects become far from being balanced. As Er decrease the abnormal nematic states in the TW mode move towards the center line (Ref. [9] for details). Thus at the ESS-TWS transition the abnormal states also move towards the center line as Er decreases, and at the quacritical point they merge into one.

The main features of the ESS-TWS transition line are (1) the transition line connects the steady state of ESS and the periodic state of TWS, (2) there are two abnormal nematic points whose position move towards the centerline ($y^*=0.5$) as the quacritical point is approached, (3) the time period for director rotations diverges at this transition line, (4) the line separates regions of two different director behaviors [i.e., winding up of the director spatial profile (ESS) and director time rotation (TWS)].

(b) *TWS-WS transition*. As mentioned above, the TWS-WS transition is similar to that in the spatially homogeneous systems predicted by Doi theory with the closure approximation. The transition between tumbling and wagging states in a spatially homogeneous system is effected through the emergence of the abnormal nematic state [17]. Close to the tumbling-wagging transition the scalar order parameter becomes remarkably small, and at the exact transition point the abnormal nematic state emerges temporally [17]. The periodic emergence of the abnormal nematic state is due to the viscous flow effect, since there is no long range elasticity effect in spatially homogeneous systems. At the TWS-WS transition line of the spatially inhomogeneous system, this abnormal nematic state temporally appears in the entire bulk region. While the bulk region experiences the transition from tumbling to wagging state, there is no major change in the boundary layer region, in which the system shows the wagging behavior in both TWS and WS regimes. It should be mentioned that this transition line separates two periodic flow regimes, and hence the transition also appears as periodic. The main features of the TWS-WS transition line are (1) the transition line separates the periodic TWS mode and the periodic WS mode, (2) the abnormal nematic state which is driven by the viscous flow effect temporally fills the bulk region, while no major change appears in the two boundary layer regions, (3) the bulk core region containing the periodically emerging abnormal nematic state shrinks as the quacritical point is approached on the De-Er (or R-Er) parametric plane, (4) this is the only transition at which the system shows periodic behavior.

(c) *WS-VSS transition*. The WS-VSS transition also has the same nature as the wagging-aligning transition in the spatially homogeneous system [17]. The amplitude of the wagging oscillation becomes zero at this transition line. In other words, the zero limit of the wagging oscillation amplitude is the flow aligning state. Both the bulk and boundary layer regions experience the transition from the oscillatory to the stationary state. The main features of the WS-VSS transition are (1) the transition line separates the periodic WS mode from the steady VSS mode, (2) the bulk core region

shrinks and the time period diverges as the quacritical point is approached on the De-Er (or R-Er) parametric plane.

(d) *ESS-VSS transition*. The ESS-VSS transition line, corresponds to a smooth continuous transition between two different steady state modes. Since the transition is continuous, both modes are equivalent and identical at the transition line. As discussed in Sec. III A the major difference between ESS and VSS is in the mechanism to achieve a steady state. In VSS, there is a bulk region where the viscous flow effect is dominant and the flow-aligning dynamics of the Doi theory is retained, and two orientation boundary layers arise to allow for the continuous changes between the flow-aligning director angle and the fixed director surface orientation. On the other hand, in the ESS mode there is no boundary layer behavior because flow alignment does not exist in this mode. To characterize this transition more clearly, we use the reactive parameter λ, which present the ratio of the strain to vorticity effects on the director [6]. For the present model, the parameter λ written in terms of the scalar order parameters S and P is given by

$$\lambda = \frac{\beta\left(4+2S+2P-S^2-\frac{1}{3}P^2\right)}{6S-2P}, \tag{9}$$

where, for $\lambda<1$ the homogeneous system adopts a nonaligning flow mode, and for $\lambda\geqslant 1$ the homogeneous system adopts the flow-aligning mode [19]. In the present spatially nonhomogeneous model $\lambda=\lambda(R,\mathrm{Er},y^*)$ and since orientation and order are coupled, it is found that λ is a function of the director angle θ.

Figure 11(a) shows the centerline director orientation $\theta(y^*=0.5)$ as a function of Er, for $R=3$ (solid line), 1 (dotted line), and 0.1 (dashed line). The director orientation displays a single undershoot followed by a monotonic increase and finally saturation to values closer to zero as R increases. The minimum is an increasing function of R, and thus higher R produces deeper wells, allowing the director to sample larger negative angles. At a R-dependent critical value Er*, the director at the centerline achieves a minimum, signaling an exchange in flow mechanisms. At Er<Er*, increasing Er produces stronger deviations from the flow direction, denoting the increasing effects of vorticity with increasing Er. On the other hand when Er>Er*, as Er increases the director aligns progressively close to the flow direction, denoting the increasing aligning tendency due to strain. Thus we have shown that the left side of the well corresponds to ESS and the right side to VSS. Next we show that the analysis is indeed corroborated by the corresponding behavior of the reactive parameter λ at the centerline $(y^*=0.5)$ as a function of Er for the chosen R values. Figure 11(b) shows the reactive parameter λ at the center line $(y^*=0.5)$ the as a function of the Ericksen number Er, for R values corresponding to the previous figure. The figure shows that the reactive parameter exhibits overshoot behavior followed by a monotonic decrease and final saturation to values increasingly greater than one for increasing R. The peaks of the overshoot increase with increasing R and occur at smaller Er values. The λ overshoots are directly correlated to the undershoots of θ, shown above. Thus very close to Er* where θ at the center line attains its minimum the reactive parameter attains its maximum which is greater than 1, thus explaining the ESS-VSS transition, simply as a change of behavior at a critical Er=Er*. For spatially nonhomogeneous system, the reactive parameter λ is a function of position and thus the aligning-nonaligning transition condition for spatially homogeneous systems, $\lambda=1$, is not exactly obeyed. Figure 11(c) shown the reactive parameter λ at the center line $(y^*=0.5)$ as a function of the director center line angle $\theta(y^*=0.5)$, for $R=3$ (solid line), 1 (dotted line), 0.1 (dashed line), and for the spatially homogeneous flow-aligning state (double dotted

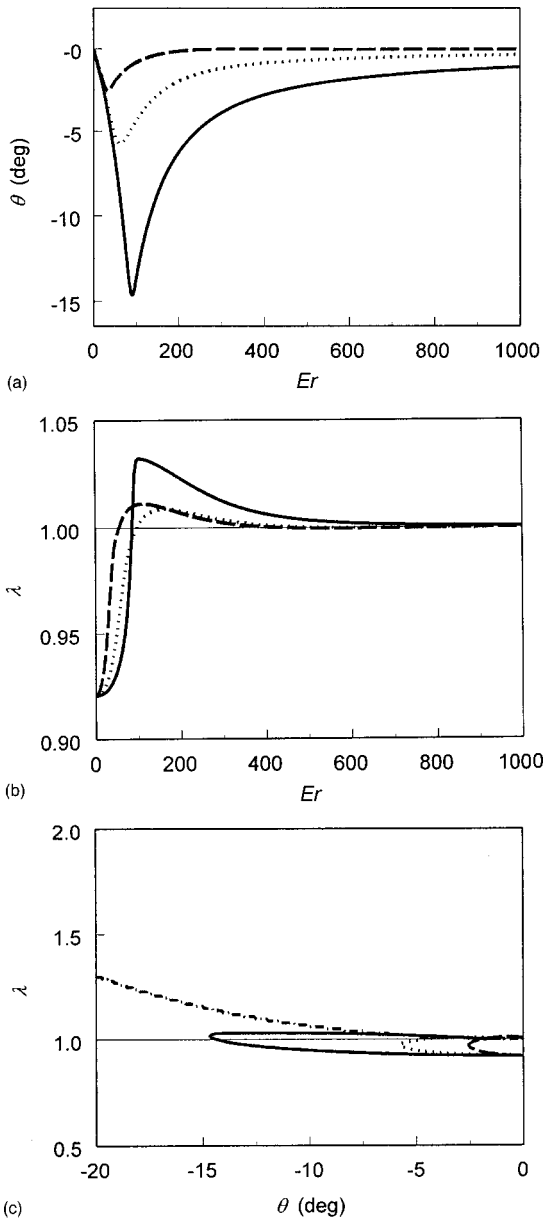

FIG. 11. (a) Director angle θ at the centerline $(y^*=0.5)$ and (b) reactive parameter λ at the center line $(y^*=0.5)$ as a function of Er, for $R=3$ (solid line), 1 (dotted line), and 0.1 (dashed line), (c) reactive parameter at the center line $(y^*=0.5)$ as a function of θ at the center line $(y^*=0.5)$, for $R=3$ (solid line), 1 (dotted line), 0.1 (dashed line), and for the spatially homogeneous case (double dotted line), respectively. For the spatially homogeneous case $\lambda=1/\cos 2\theta$.

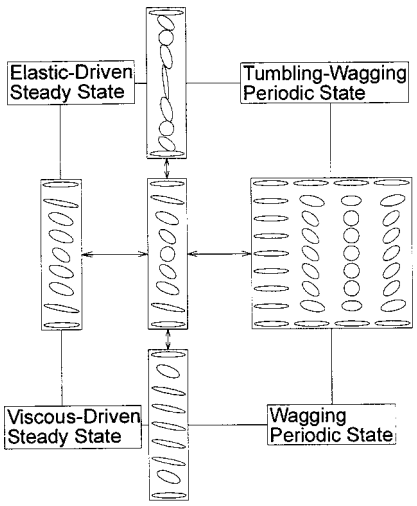

FIG. 12. Schematic of the tensor parameter profiles at four transitions (ESS-TWS, TWS-WS, WS-VSS, and VSS-ESS) as well as at the quacritical point (at the center). The ellipsoids show the tensor order parameter states and the role of the abnormal nematic states at the transitions and at the quacritical point. See text.

line). The lines are obtained by increasing Er from zero; increasing Er from zero corresponds to left motion along the curves towards the turning point and subsequently to the right. The thin solid line represents the critical $\lambda = 1$ transition value for homogeneous systems. The spatially homogeneous flow-aligning state profile is given by the Leslie angle θ_L relation [6]

$$\lambda = \frac{1}{\cos 2\theta_L}.$$

As Er increases from zero all the curves are below 1 and the mode is ESS. At a critical Er* a turning point is found and further increases of Er increase θ and therefore λ such that flow-alignment emerges. The exact location of the turning point is not exactly one because the system is spatially nonhomogeneous. As R increases the nonhomogeneous effects on the VSS decreases and thus the predicted λ curves for the flow-aligning branch becomes closer and closer to the classical Leslie value. The major features of the ESS-VSS transition line are (1) the transition line connects two steady states of ESS and VSS and (2) at the line, the effective reactive parameter is equal to 1.

(E) *Quacritical point*. The quacritical point must be compatible with all of the four transition lines, since all the transition lines emerge from this point, as shown in Figs. 8 and 9. Such high order transition points are well known in equilibrium thermodynamic systems [18]. From the features of the four transition lines, it follows that at this point, the system has an abnormal nematic state at the centerline and the orientation field is stationary. Since the abnormal nematic state introduces a vector singularity to the system, the director dynamics is undefined and it is possible to display a tensor order parameter state that is fully compatible with all the four flow states.

Figure 12 shows a schematic of the tensor parameter profiles at the transitions as well as the quacritical point (at the center). Each schematic between the boxed text represents the tensor ellipsoid profiles between the two indicated flow regimes. Recall that a circle denotes the abnormal nematic states. For example the transition between the TWS and WS is effected through the periodic emergence of an abnormal nematic bulk layer. The other remaining schematics follow directly from the previous discussions. At the center of the figure the schematic of the tensor order parameter at the quacritical state is shown to be fully compatible with the space and time dependent structural characteristics of the tensor order parameter profiles at all the four flow transitions. Thus the figure provides a synthesis and a consistent unified vision of spatially nonhomogeneous planar nematorheology in the presence of short- and long-range elasticity.

TABLE I. Characterization of flow-mode transitions. ESS: elastic-driven steady state, TWS: tumbling-wagging composite state, WS: wagging state, and VSS: viscous-driven steady state. Hard: discontinuous change; Soft: continuous change.

	ESS-TWS	TWS-WS	WS-VSS	ESS-VSS
Amplitude of director dynamics	Hard	Hard	Soft	Soft
Time period of director dynamics	Soft	Soft	Hard	Soft
Boundary layer thickness	Hard	Soft	Soft	Soft

Finally, the four transition states are classified in Table I, using the standard way to characterize transition phenomena in nonlinear systems [20]. While the time period and amplitude are used to classify temporal systems, for spatiotemporal systems one more parameter is required to fully characterize the spatial behavior. We chose the boundary layer thickness for the spatial characterization, and it is the most reasonable quantity for this purpose. The change in these three quantity (i.e., the amplitude, period, and boundary layer thickness) is qualified in terms of soft and hard transitions, which corresponds to continuous and discontinuous changes in these quantities. For example, the ESS-TWS transition is hard in both amplitude and boundary layer, but soft in the period. The change in amplitude of the director dynamics is hard because ESS is a steady state and TWS a periodic state, the period is soft because at the transition the period of TWS diverges, and in terms of boundary layer it is hard because the steady ESS mode has no boundary layer behavior but the TWS mode does, since it has two wagging surface layers. The entries in the other columns can be explained in similar ways.

IV. CONCLUSIONS

In this paper we have simulated the in-plane shear flows of LC materials using a theory whose asymptotic limits were previously shown to be the Leslie-Ericksen theory ($R \to \infty$) and the Doi theory with a closure approximation ($\mathrm{Er} \to \infty$). It is shown that the present theory predicts four orientation flow modes: (1) an elastic-driven steady state, (2) a composite tumbling-wagging state, (3) a wagging state, and (4) a viscous-driven steady state. The elastic-driven steady state is similar to the LE solution for nonaligning nematics [14], where the long-range elasticity effect is dominant over the

entire flow geometry, and thus the orientation field is stabilized by the fixed director at the walls. The composite tumbling-wagging (TWS) mode consists of a tumbling core with two wagging surface layers. If the long-range elasticity is neglected this mode becomes identical to the tumbling solutions of the Doi theory. The wagging (WS) mode is an oscillatory solution, in which the amplitude of the oscillation decreases from a maximum at the centerline to zero at the bounding surfaces. The WS mode becomes identical to that predicted by Doi's theory if long-range elasticity is neglected. Lastly, the present theory predicts a viscous-driven steady state (VSS), arising from the flow aligning behavior that exists at relatively high Er. The VSS is spatially inhomogeneous and is similar to the LE solutions for flow-aligning nematics, and the core region is similar to the steady state predicted by Doi theory with the closure approximation.

The present theory smoothly fills the entire gap between the well-known Leslie-Ericksen and Doi theories for flowing liquid crystals. The complete in-plane orientation flow phenomena of nematic liquid crystalline materials is established by the rheological phase diagram spanned by R and Er, and also De and 1/Er. Four transition lines in the parametric plane that define the stability regions for the four (ESS, TWS, WS, VSS) flow regimes are shown to converge at a quacritical point which exhibits the structural characteristics of the four modes. The most significant feature of the quacritical point is the presence of the steady abnormal nematic state. At the abnormal nematic state, not only the director itself but also its dynamics are undefined. So that, one can regard the director dynamic at this state as stationary, rotational, and oscillatory, but only on the order parameter tensor level the abnormal nematic state is stationary. The reason why this discrepancy occurs is that the characterization of the flow regime is based on vector level director dynamics which can not fully describe the tensor level orientation dynamics. Even if the scalar order parameter is taken into account, vector equations are not applicable to the abnormal nematic state. Thus, at least a second order tensor level description of the orientation field is required for fully describing the nonlinear flow phenomena of LC materials.

ACKNOWLEDGMENTS

One of us (A.D.R.) gratefully acknowledges the financial support from the Natural Science and Engineering Research Council of Canada.

APPENDIX

When $R\rightarrow\infty$ the present theory is compatible with the Leslie-Ericksen theory. In this case, the system keeps the scalar order parameter at the equilibrium value S^{eq}. Thus, the order parameter tensor is written by

$$\mathbf{Q}=S^{eq}\left(\mathbf{nn}-\frac{\delta}{3}\right). \tag{A1}$$

Using this uniaxial description for $\mathbf{Q}$, the present theory can be reduced to

$$S^{eq}\frac{\partial\mathbf{n}}{\partial t}=\frac{1}{S^{eq}\eta}\frac{\delta F}{\delta\mathbf{n}}+S^{eq}\mathbf{W}\cdot\mathbf{n}+\beta\left(\frac{2}{3}+\frac{1}{3}S^{eq}-\frac{1}{6}S^{eq^2}\right)\times(\mathbf{A}\cdot\mathbf{n}-\mathbf{nn}\cdot\mathbf{A}\cdot\mathbf{n}), \tag{A2}$$

where F is the Frank energy (see Ref. [11] for details). Thus,

$$\gamma_1\frac{\partial\mathbf{n}}{\partial t}=\frac{\delta F}{\delta\mathbf{n}}+\gamma_1\mathbf{W}\cdot\mathbf{n}+\gamma_2(\mathbf{A}\cdot\mathbf{n}-\mathbf{nn}\cdot\mathbf{A}\cdot\mathbf{n}), \tag{A3}$$

where

$$\gamma_1=S^{eq^2}\eta,\gamma_2=\beta\left(\frac{2}{3}+\frac{1}{3}S^{eq}-\frac{1}{6}S^{eq^2}\right)S^{eq^2}.$$

Note that the rotational viscosity γ_1 is proportional to S^2 as previously reported [6].

[1] G. Marrucci and F. Greco, Adv. Chem. Phys. **LXXXVI**, 331 (1993).
[2] M. Doi, J. Polym. Sci., Polym. Phys. Ed. **19**, 229 (1981).
[3] M. Doi and S. F. Edwards, *The Theory of Polymer Dynamics* (Clarendon Press, Oxford, 1986).
[4] R. G. Larson and H. C. Ottinger, Macromolecules **24**, 6270 (1991).
[5] F. M. Leslie, *Theory of Flow Phenomena in Liquid Crystals. Advances in Liquid Crystals* (Academic, New York, 1979), p. 1.
[6] P. G. deGennes, *The Physics of Liquid Crystals* (Clarendon Press, Oxford, 1974).
[7] A. N. Beris and B. J. Edwards, *Thermodynamics of Flowing Systems* (Oxford University Press, Oxford, 1994).
[8] R. G. Larson, *Constitutive Equations for Polymer Melts and Solutions* (Butterworths, London, 1988).
[9] T. Tsuji and A. D. Rey, J. Non-Newtonian Fluid Mech. **73**, 127 (1997).
[10] A. D. Rey, Macromol. Theory Simul. **4**, 857 (1995).
[11] M. J. Stephen and J. P. Straley, Rev. Mod. Phys. **46**, 617 (1974).
[12] N. C. Andrews, B. J. Edwards, and A. J. McHugh, J. Rheol. **39**, 1161 (1995).
[13] A. D. Rey, Macromolecules **24**, 4450 (1991).
[14] P. Manneville, Mol. Cryst. Liq. Cryst. **70**, 223 (1981).
[15] A. Sonnet, A. Kilian, and S. Hess, Phys. Rev. E **52**, 718 (1995).
[16] G. Marrucci, Macromolecules **24**, 4176 (1991).
[17] Y. Farhoudi and A. D. Rey, J. Rheol. **37**, 289 (1993).
[18] L. D. Landau and E. M. Lifshitz, *Statistical Physics*, 3rd ed. (Pergamon, Oxford, 1990), Pt. I, p. 497.
[19] R. G. Larson, Macromolecules **23**, 3983 (1990).
[20] A. V. Gaponov-Grekhov and M. I. Rabinovich, *Nonlinearities in Action* (Springer-Verlag, Berlin, 1992).